Localized Near Surface Temperature Inversion Forecasting using Long Short-Term Memory

Taylor Dinkins[1], Weng-Keen Wong[1], Basavaraj Amogi[2], Paola Pesantez-Cabrera[2], Jaitun Patel[2], Lav Khot[2], Alan Fern[1]

[1]Oregon State University
[2]Washington State University
dinkinst@oregonstate.edu, wongwe@oregonstate.edu, basavarajamogi@gmail.com, p.pesantezcabrera@wsu.edu, jaitun.patel@wsu.edu, lav.khot@wsu.edu, alan.fern@oregonstate.edu

Abstract

Near surface temperature inversions are periods in which a low layer of warm air is trapped between cooler air higher up in the atmosphere and dense cooler air below it near the surface level. By causing cooler air to pool near the surface level, inversions can have detrimental effects for crop growers, including frost, increased moisture, and pesticide drift. As a result, predicting the occurrence and magnitude of these inversions yields substantial benefits for growers. We introduce a Long Short-Term Memory (LSTM) model for temperature inversion forecasting that is able to effectively predict localized, near surface temperature inversions in advance such that growers can take actions to mitigate the detrimental effects. We show a substantial performance gain over a deployed temperature inversion forecasting system, and include a series of ablations that show the benefit of using publicly available terrain-specific feature information when modeling inversions at this scale.

1 Introduction

Under normal conditions, air temperature decreases when elevation increases. A *temperature inversion* occurs when a layer of warmer air traps colder air below it, thereby inverting the relationship between temperature and elevation. Temperature inversions can have significant impact in numerous ways as they are known to degrade air quality by trapping pollutants (Xu et al. 2019), cause challenges for aircraft pilots (Dennstaedt 2023) and change ecosystem processes (Novick, Oishi, and Miniat 2016).

The focus of this work is on the effects of temperature inversions on agriculture, specifically those inversions which occur near ground surface level. One common example of the impacts these inversions have is when the lower surface temperatures cause frost to form, which can damage crops (Bates, Lombard et al. 1978; Ohlemeier 2025). Additionally, temperature inversions can cause spray drift, in which pesticides spread over a much larger area than their intended target (Bish, Guinan, and Bradley 2019). Predicting the occurrence of local temperature inversions is thus of critical importance (Gommes et al. 2010) since farmers can often proactively mitigate the consequences. For instance, in the presence of sufficiently strong inversions (2°F or greater), wind machines can be turned on to mix the warm air with the cold air and raise the temperature for crops up to approximately half of the inversion strength temperature (Amogi, Khot, and Hill 2024; Bates, Lombard et al. 1978; Prengaman 2025).

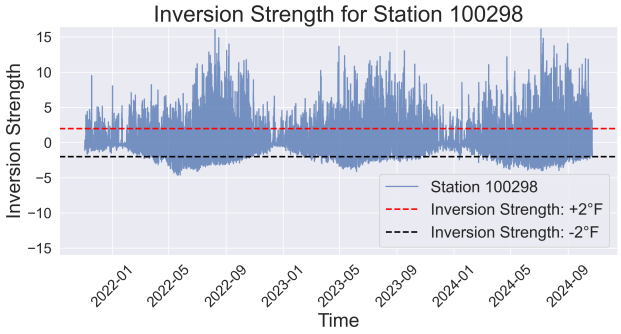

Figure 1: Plot of inversion strength over time for AWN station ID `100298`

Near surface temperature inversions depend on many measurable factors including elevation, land cover, landscape topology, the current air temperature, solar radiation, and wind speed. Temperature inversions also exhibit strong seasonal and daily cyclical patterns (Abdul-Wahab et al. 2004; Noad et al. 2023; Riordan, Davis, and Kiess 1986; Rupp et al. 2020). Weather station networks such as AgWeatherNet (AWN) (Amogi, Khot, and Hill 2024; Amogi, Khot, and Hoheisel n.d.) can detect the occurrence of near surface level temperature inversions in effectively real-time. Air temperature sensors installed at different heights (e.g. one at 1.5 meters and another sensor at 9 meters from a tower station) can flag an inversion at a station if the higher sensor reports a warmer temperature than the lower one.

A challenging task is to predict the occurrence of a *localized* temperature inversion in the near future using the historical sensor measurements at one or more weather stations. Our work investigates the potential for using sequential deep neural network models, specifically Long Short-Term Memory models, along with common weather variables and terrain features, to predict station specific temperature inversions at a near surface height.

2 Related Work

The majority of existing work on modeling temperature inversions (Abdul-Wahab et al. 2004; Burger, Gubler, and Brönnimann 2022; Helbig et al. 2021; Hiscox et al. 2023; Hudson and Brandt 2005; Joly and Richard 2022a,b; Lagmiri and Dahech 2024; Noad et al. 2023; Ramsey and Monahan 2022; Rendón et al. 2014; Xu et al. 2021; Zhang, Zhang, and Yang 2022; Zhang et al. 2025b) involve the analysis and characterization of temperature inversions at the lower atmosphere, which includes a much larger vertical range than the near-surface level we are concerned with in our work. Notably, surface-based inversions themselves appear to have increased from 1989 to 2019 (Zeng et al. 2022), spurring researchers to explore this issue further.

Data for detecting temperature inversions is commonly obtained through remote sensing or by radiosonde, which is an instrument carried on a weather balloon. This data is used to produce a vertical profile of how air temperature varies with increased elevation, thereby enabling the characterization of temperature inversions. A variety of different machine learning methods have been applied to these types of data to create vertical profiles for temperature and we briefly mention examples of deep learning approaches. (Ma et al. 2021) use a deep neural network and satellite measurements to improve the lower level profiling of NUCAPS, the satellite sounding system from the National Oceanic and Atmospheric Administration. This work operates on a spatial resolution of 45 kilometers and a temporal resolution of 12 hours, which is typical for sounding data sources. (Haynes et al. 2024) use a U-Net model and satellite data to post-process existing numerical weather prediction model forecasts for improving the vertical profiling of temperature and moisture, and overcoming the 12 hour sampling rate for the radiosondes. These vertical profiles could be used to compute inversions at specific heights; however they use 256 vertical levels, up to an altitude 17 kilometers, and the approximate resolution for each vertical level would be 66 meters. (Wu et al. 2024) use an LSTM and a mathematical background field model of historical climate data for forecast correction on temperature inversions at vertical intervals in China's Taizhou City. This work operates on data collected at a 12 hour sampling rate, and a height resolution of 100 meters, up a 10 kilometer altitude.

This body of literature is tackling a fundamentally different problem from our work in three aspects. First, our work focuses specifically on modeling temperature differences between two near surface temperature sensors, rather than building a vertical profile of temperature much higher up in the atmosphere. Second, our spatial and temporal scales are much smaller as we are concerned with local rather than regional areas and we operate at an hourly granularity. The stations we consider are spaced approximately 30 kilometers apart from the nearest spatial neighbor, and our forecasting focuses on a the immediate station vicinity, as many of these stations are placed on or near farms. Our work is not intended to function at a large regional scale, but rather to capture the variations within.

A different but related area involves the prediction of the height of the Planetary Boundary Layer, which is defined as the "the lowest layer of the troposphere where wind is influenced by friction" (Haby 2024). The top of this layer is often marked by the presence of a temperature inversion, and the height of this layer is driven in part by the surface temperature of the Earth. This height generally ranges from 100 to 2000 meters (Pielke Sr 2013). Various papers attempt to predict this Planetary Boundary Layer Height (PBLH), such as (Chu et al. 2025; Kumar, Soni, and Agarwal 2021; Milstein, Santanello, and Blackwell 2023; Silva et al. 2025; Su and Zhang 2024; Yang et al. 2023; Zhang et al. 2025a) .

Of particular interest is: (Su and Zhang 2024), which predicts the PBLH using a deep neural network trained on radiosonde and lidar meteorological measurements. A survey of additional machine learning methods in Planetary Boundary Layer related tasks can be found in (Canché-Cab et al. 2024). In contrast to these methods, we operate exclusively at a near surface altitude ($\leq$ 9 meters) and provide localized point forecasting for temperature inversions at individual station locations, rather than at the PBLH.

To our knowledge, there is no existing work that directly addresses the specific problem of near surface inversion strength prediction on a local scale other than the approach described by (Amogi, Khot, and Hill 2024; Amogi, Khot, and Hoheisel n.d.) implemented in the AWN system, which we evaluate against in our experiments.

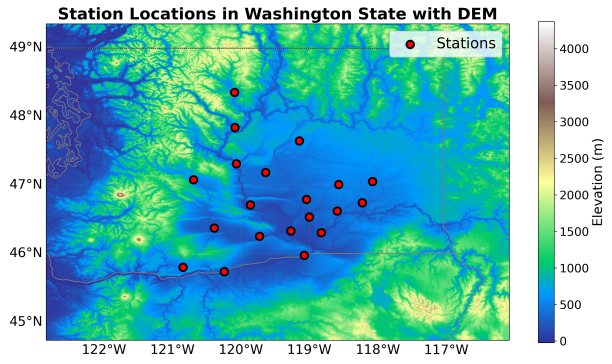

Figure 2: Station locations shown as red dots in Washington State.

3 Methodology

3.1 Data

Let $\boldsymbol{X}_{1:T} \in \mathbb{R}^p$ be a multivariate time series of p features. Our goal is to predict the near surface inversion strength at time $t+k$, given some sequence of historical data $\boldsymbol{X}_{(t-i):(t-j)}$, for some $i > j$. With θ^{1m} as the air temperature measurement at 1 meter height, we define this inversion strength S_t at time t as

$$S_t = \Delta(\theta)_t = \theta_t^{9m} - \theta_t^{1m} \tag{1}$$

A plot of S_t for AWN station ID `100298` is shown in Figure 1. As illustrated, inversions vary in duration and magnitude, follow seasonal patterns, and are more frequent during the colder months at this station. The presence of many inversions $\geq 2^\circ F$ are common. We predict S_t directly, rather

than predicting θ_t^{9m} and θ_t^{1m} separately, to avoid the issue of compounding errors resulting from two separate forecasts. We use the AWN project from Washington State University (WSU) as a test-bed for inversion prediction, and use various sensor measurements from each station to perform direct inversion forecasting. AWN has an existing temperature inversion prediction model, and we define our experiments to operate with similar conditions to make a direct comparison possible. Currently, we restrict ourselves to stations located in climate zones 7 and 8. These zones comprise the Yakima Valley in Washington state, which grows the largest variety of produce in the Pacific Northwest United States. Figure 2 shows a map of these 20 unique stations in Yakima Valley.

We pre-process the data in a standard manner and ensure hourly temporal continuity by linearly imputing missing data and obvious out-of-bounds measurements, such as those with air temperature values outside of the range $[-35^\circ F, 125^\circ F]$, values nearing ∞, or sensor error codes of sequences of 9's. We add a quality control "missing" binary flag for time stamps that required imputation. We have a set of weather variables from AWN we use as predictors, with the response variable being the near surface temperature inversion strength. A positive value for this inversion strength, $S > 0$, implies the presence of a temperature inversion from 1 meters to 9 meters above the surface. A negative or zero value, $S \leq 0$, indicates that no inversion is currently present.

For inversion strength prediction, we highlight two important types of features which we include in our model. The first is a set of features from neighboring stations, which should provide valuable information since nearby stations are likely affected by similar weather patterns. We define, for any given station, its nearest neighbors based on correlation across stations. We use the seasonally adjusted AIR_TEMP_1M_F feature across our training window, and compute 2 nearest neighbors (2-NN) for each station as those additional stations with the highest Pearson correlation across this window. We concatenate the 2-NN features at the same time index with those of the current station's, effectively tripling the size of the feature space. We chose to use the 2 nearest neighbors because neighboring weather stations in the AWN are far apart in the Yakima Valley relative to the spatial behavior of inversions we wish to capture.

A second set of features that we include are a set of terrain features. We collect these features from the United States Geological Survey (USGS) 10 meter resolution Digital Elevation Models (DEM) dataset (Survey 2021) using OpenTopography, and a histogram of 20 land cover types from the National Land Cover Database (NLCD) 2023 for an approximately 4km x 4km region centered on each station (Survey 2024). DEM files capture elevations values within a spatial grid, and we derive 7 coarse-grained summary features using the RichDEM Python package (Barnes 2016) from the DEM for each station using the exact latitude and longitude of the station. We calculate a further 7 of the same features using the median of a 3x3 grid window centered on the station. We concatenate these, along with time-of-day and month-of-year features to the station data and those measurements of its 2 nearest neighbors. There is an open question of what representation of the DEM proves most effective for incorporating terrain in machine learning models. Here we have used derived features common in geospatial modeling. In Section 4.2, we consider briefly using a learned representation from the DEM using convolutional neural networks, which has the potential to capture more predictive aspects of the terrain.

We highlight that we do not make use of 9 meter air temperature, AIR_TEMP_9M_F, as an input feature, nor any other tower station sensor readings when these are available for any station. A long-term goal for this model is to eventually provide forecasts for stations without tower readings, so we make this modeling assumption up front. The only place we use the 9 meter air temperature is establishing ground truth response values (i.e. actual inversion strength measurements) during evaluation and training.

3.2 Model

Recurrent neural networks (RNNs) are types of neural network models designed to operate on sequential data. These networks maintain a hidden state that is updated at time step t as a function of the current input $\boldsymbol{X}_t$ and the previous hidden state $\boldsymbol{h}_{t-1}$. Long Short-Term Memory (LSTM) (Hochreiter and Schmidhuber 1997) is a specific type of RNN that relies on a "cell state" and gating mechanisms for controlling the flow of information into and out of the cell over time. These networks have been used extensively in many domains, such as speech recognition, time series forecasting, and language translation.

We use an autoregressive, encoder-decoder architecture (Sutskever, Vinyals, and Le 2014) to predict temperature inversions. Here, an encoder network processes some sequence of historical data into a representation, and the decoder then uses this representation and its own previous outputs to produce a sequence of predictions one step at a time. Both the encoder and decoder use LSTM units in order to capture the temporal dynamics present in the remote sensing data. Additionally, we include temporal attention (Vaswani et al. 2017) in the encoder to encourage the model to focus on the most relevant time steps of the historical input sequence. Figure 3 provides a diagram of the model.

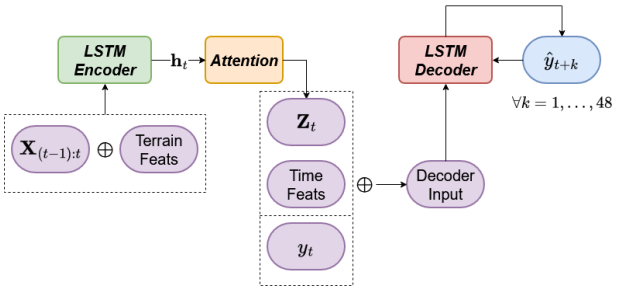

Figure 3: Autoregressive LSTM model diagram for temperature inversion forecasting. $\boldsymbol{Z}_t$ is the representation context vector generated by the encoder, and used for priming the decoding. ($\oplus$ denotes the concatenation operator, and the 2-NN features are included in $\boldsymbol{X}_{(t-1):t}$.)

Feature Name	Description	Source
Air Temperature 1m	Air temperature at 1 meter above ground level (°F)	AWN[1]
Elevation	Ground elevation above sea level (ft)	AWN[1]
Relative Humidity	Relative humidity percentage (%)	AWN[1]
Dew Point	Dew Point temperature value (°F)	AWN[1]
Precipitation	Precipitation rate (in/hr)	AWN[1]
Wind Speed	Wind speed at 2 meters height (mph)	AWN[1]
Wind Gust	Wind gust at 2 meters height (mph)	AWN[1]
Solar Radiation	Solar radiation strength (mJ/m^2)	AWN[1]
Soil Temperature 2in	Soil temperature at 2 inch depth (°F)	AWN[1]
Soil Temperature 8in	Soil temperature at 8 inch depth (°F)	AWN[1]
Month (One-Hot)	Month of year as one-hot vector (12 dimensions)	AWN[1] Timestamp
Hour (One-Hot)	Hour of day as one-hot vector (24 dimensions)	AWN[1] Timestamp
Missing	Binary missing indicator for Air Temperature 1m	AWN[1]
Slope	Local terrain slope (degrees, [0°, 90°])	USGS[2] DEM
Slope Rise/Run	Local terrain rise/run (percentage)	USGS[2] DEM
Aspect	Terrain aspect (slope facing degrees from north, clockwise)	USGS[2] DEM
Curvature	Change in slope (convexity (+)/concavity(−))	USGS[2] DEM
Profile Curvature	Curvature along direction of maximum slope	USGS[2] DEM
Plan Curvature	Curvature perpendicular to direction of maximum slope	USGS[2] DEM
Hillshade	Sunlight illumination of surface from direction 315° and height 45° ([0,1], shadow to shade)	USGS[2] DEM
Landcover Histogram	Counts of landcover types in region (20 types)	NLCD 2023[3]

[1]https://weather.wsu.edu/ [2]https://doi.org/10.5069/G98K778D [3]https://doi.org/10.5066/P94UXNTS

Table 1: Summary of dataset features with descriptions and sources.

4 Results and Discussion

For our experimental setup, we use the 20 field-deployed weather stations in Yakima Valley, operated by AWN, each of which does have a tower station - though as before, we do not use tower station data as predictor variables. Figure 2 has a view of the station latitude/longitude positions. We set the training data to be the entire history of readings in which a station has 9 meter temperature measurements collected, which is necessary for the ground truth inversion strength calculation. Note that this can be a variable timeframe across the different stations, and some stations do not have available training data and are used only during validation. The training data is from the earliest June 16th, 2021, through October 31, 2023 - again, some stations do not have data as early as 2021. The validation data runs from November 1st, 2023 through October 22, 2024. As inversions exhibit strong seasonal patterns, it is important to have a representation of all seasons in the validation data. We use the data sampled at the top of each hour, for 24 readings per day.

We define our encoder-decoder model using LSTM units with two hidden layers, with the embedding size of 256, and dropout (Srivastava et al. 2014) of 0.2 inside the units and 0.3 before final prediction in the decoder. During training, we use the Adam optimization algorithm (Kingma and Ba 2017) with a learning rate of $5e^{-4}$, a batch size of 256 sequences, and set a maximum of 30 epochs. During training we apply linearly decayed teacher forcing (Williams and Zipser 1989) from 0.9 to 0.05 up to 15 epochs. We use the root mean-squared error (RMSE) as the loss function.

We use a sequence length of 72 hours worth of data for the encoder, after which we unroll the decoder to make hourly predictions up to 48 hours out. Since localized forecasts tend to degrade as the horizon increases, we choose to focus on the 48 hour time frame as it is suitable for actionable decision-making by growers, who will typically be able to minimize the effects of the inversion around 24 hours prior (Amogi, Khot, and Hoheisel n.d.; Prengaman 2025).

4.1 AWN Comparison

AWN has a deployed near surface temperature inversion forecasting system based on multivariate regression that is available to users, which provides localized forecasts at each station. These forecasts are made four times a day, out to a horizon window of 10 days at an hourly resolution. We restrict our forecast window to be 48 hours out, in line with our model training, and align our forecasts with those of the AWN system in station ID, starting and ending timestamp, and forecast horizon. Over the validation window, the AWN forecasts comprise only 12 out of the 20 stations, even though measurements were present at the additional 8. These IDs are: `[100298, 100300, 100308, 100310, 100331, 100357, 100367, 100368,`

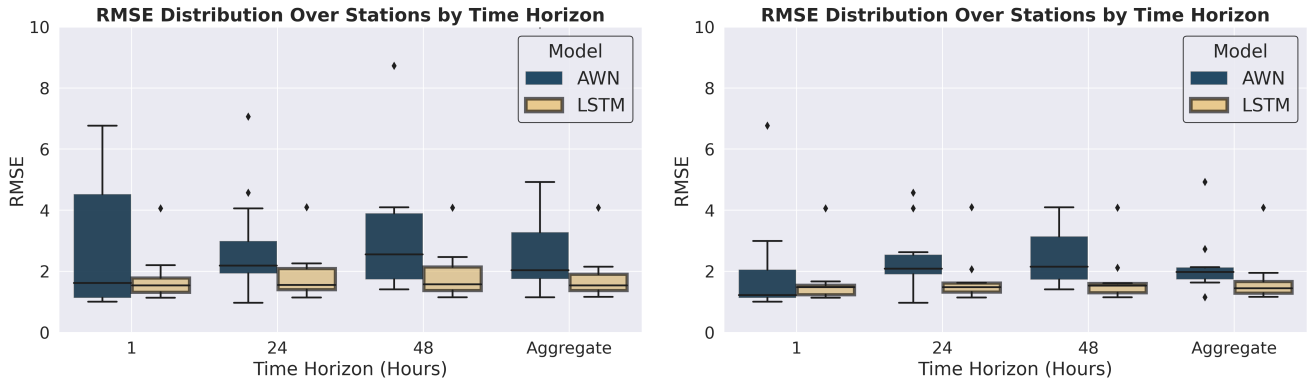

Figure 4: Distributions of the RMSE values at the specified time horizons for the best performing LSTM model and the AWN system. **Left:** Over the 9 stations. **Right:** Over the 7 stations, excluding the poor performers for AWN. The "Aggregate" is the average over all stations and all hourly forecasts horizons from 1 to 48. ⋄ symbols indicate outliers.

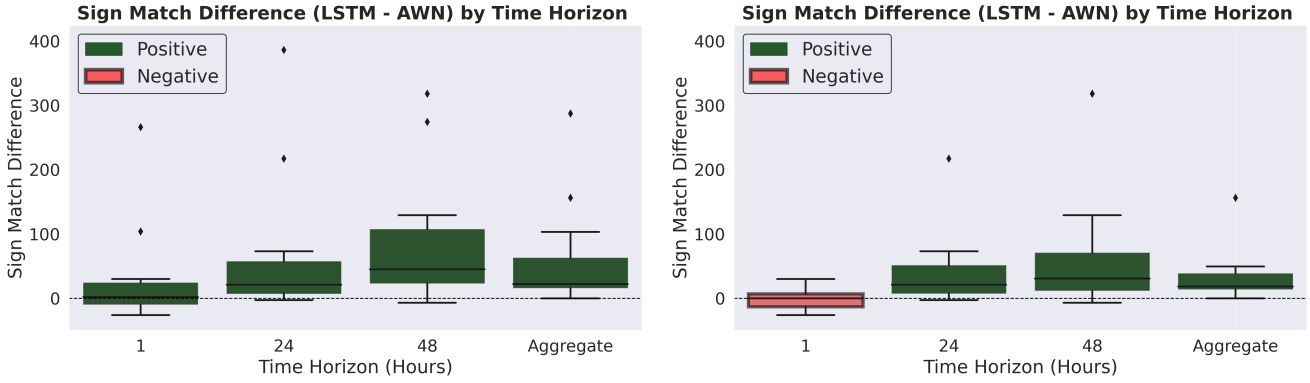

Figure 5: Sign match difference for best performing LSTM model and AWN at the specified time horizons. **Left:** Over the 9 stations. **Right:** Over the 7 stations, excluding the poor performers for AWN. Green indicates a greater number of correctly signed predictions by the LSTM. Red indicates a greater number of correctly signed predictions by AWN. The "Aggregate" is the average over all stations and all hourly forecasts horizons from 1 to 48. ⋄ symbols indicate outliers.

Time Horizon	S	N	ST	NT	ST-NLCD	NT-NLCD	ST-NLCD-DEM	NT-NLCD-DEM
Aggregate	1.672	1.699	1.662	1.639	1.647	**1.633**	1.638	*1.631*
1 Hour	1.444	1.516	1.565	1.410	1.424	**1.394**	1.445	1.400
24 Hours	1.721	1.757	1.704	1.685	1.691	**1.684**	*1.676*	1.685
48 Hours	1.788	1.789	1.747	1.736	**1.733**	**1.733**	*1.729*	*1.726*

Table 2: Feature Ablations - RMSE values for the best performing LSTM with each set of features. **Bold** indicates best performing set of features.
S: Single station, **N**: Neighbor features, **T**: Terrain features, **NLCD**: NLCD histogram, **DEM**: Full DEM file. *Emphasized* in the right columns indicates an improvement with the CNN DEM file processing over the identical setting without it. "Aggregate" is the average over all stations and all hourly forecasts horizons from 1 to 48.

310031, 330035, 330040, 330115]. AWN only provides forecasts for stations after they are installed for one year. Stations [100310, 100331, 100357] do not have forecasts prior to April, 2024, and had a high number of forecasting errors, so we do not include them in the comparison. We note that 2 of these remaining 9 stations ([100367, 100368]) also have poor AWN forecasts, perhaps suggesting either sensor quality control issues or a need for model recalibration. In all cases, our model used all of the 20 field-deployed stations in Figure 2 with measurements available before October 31, 2023 during training. We use the AWN forecasts to identify any time points in which obvious sensor errors are present, such as those with missing data and those exceeding the range of quality control on forecast numbers for air temperature (outside the range of $[-35^\circ F, 125^\circ F]$). We drop these entire timestamps from both forecasts prior to comparisons. Note that doing so favors the AWN models as their out-of-range predictions are dropped from the evaluation.

Figure 4 shows the distribution of the RMSE of the forecasts averaged over stations, at three specific time horizons, as well as the average over all 48 time horizons as a box plot. Box plots show the quartiles of the RMSE in the box, while the whiskers extend to show the rest of the distribution. We include comparisons for the entire 9 stations on the left, and for 7 stations - with the more problematic 2 stations ([100367, 100368]) excluded - on the right. Our LSTM based model significantly outperforms the currently deployed system in both cases, at all reported time horizons.

In addition to the inversion strength prediction itself, it is useful for users to know whether an inversion will simply be present or not. That is, whether $S_t > 0$ (inversion) or $S_t \leq 0$ (no inversion). With the same assumptions of stations, we present the difference in the number of correctly signed inversion strength predictions in Figure 5. This figure shows how many more correctly signed predictions per station our LSTM makes over the AWN system. In both cases, we see a large performance gain as the time horizon increases. For predictions at 1 hour, the number of correctly signed predictions on the "stable" stations is nearly identical. In the other cases, including the aggregate over horizons, our model achieves a greater number of correct signs.

4.2 Ablation Study

Table 2 quantifies the impact of the neighbors and the terrain features through a series of ablation experiments. For each experiment, we train identical LSTM models in the manner previously specified with varying access to features from Table 1. Specifically, we include or exclude neighbor information, terrain features extracted from the USGS DEM, and the National Land Cover Database histogram. We compare these results across the same time horizons, over the same 9 stations and timestamps (with exclusions) as with AWN.

The consistently best performing setting involves the use of all features from Table 1 with AWN neighbors included. We generally see a steady improvement when adding terrain features, particularly in conjunction with neighbor information. This result highlights the use of terrain features and neighbors when modeling these inversions, and the potential for improvements when testing our model in actual deployment.

We report two additional results by processing the entire DEM file for each station through a convolutional neural network (CNN) (LeCun, Bengio, and Hinton 2015) to perform feature extraction at a dimensionality of 32. This CNN feature embedding is treated as an additional input to the LSTM decoder by concatenation with the context vector $\boldsymbol{Z}_t$, and is trained jointly. In several cases, this additional feature embedding is able to slightly improve performance over the best model performance from the counterparts without the CNN, while using the same features from Table 1. This result suggests that future investigation into other learned representations of the DEM features could be promising. Lastly, the supplementary material contains a table which lists the gradient based feature importance for the top 20 features.

5 Future Work and Conclusion

Our model is on track to be deployed on the AWN system, alongside the existing model, to provide inversion forecasts for the farmers. This will provide a performance evaluation of the LSTM in a testing and deployment setting, and we plan to collect feedback on the forecasts from the users. The deployment will also generate forecasts for stations without tower readings, which should assist farmers in decision making for these locations that did not previously have access to inversion forecasts at this scale. We plan to update the model as new stations and more historical data become available. The wall-clock time for retraining is under 4 hours, and inference time for a single forecast at all stations, relative to the resolution and horizon of the forecasts, is negligible.

For future work, we will be retraining and applying the model across the entire state of Washington. Our model is a first attempt at improving on an existing model specific to this inversion prediction task. We chose a simple way to model the informative aspects unique to our problem (e.g. neighbor information, station-level terrain features, and temporal autocorrelation) to understand the influence of these characteristics. Other more complex time series models could be used (Ansari et al. 2024; Auer et al. 2025; Beck et al. 2024; Das et al. 2024; Ekambaram et al. 2024; Wen et al. 2022), but their complexity obfuscates the initial analysis and it is uncertain if the added complexity helps. We plan to investigate if more sophisticated algorithms improve forecasting results. Specifically, we aim to make better use of neighborhood information for sensors that lie close to another, or in similar regions, through Graph Neural Networks (Jin et al. 2024). An informed use of these has the potential to track the movement of inversions, which often behave on slopes and ridges like water flowing downhill (Rupp et al. 2020). We will perform further studies specific to the model's capacity to generalize across stations without tower readings, and lastly, we will investigate a better use of the DEM files to produce other informative representations of terrain features that may guide the prediction of temperature inversions.

6 Acknowledgments

This research was supported by USDA NIFA award No. 2021-67021-35344 (AgAID AI Institute).

References

Abdul-Wahab, S. A.; Al-Saifi, S. Y.; Alrumhi, B. A.; Abdulraheem, M. Y.; and Al-Uraimi, M. 2004. Determination of the features of the low-level temperature inversions above a suburban site in Oman using radiosonde temperature measurements: Long-term analysis. *Journal of Geophysical Research: Atmospheres*, 109(D20).

Amogi, B.; Khot, L.; and Hill, S. 2024. https://treefruit.wsu.edu/article/temperature-inversion-forecasts-available-for-agweathernet-mesonet-tower-stations/.

Amogi, B.; Khot, L.; and Hoheisel, G. n.d. Washington State University. https://treefruit.wsu.edu/article/a-new-tool-to-estimate-inversion-strengths/.

Ansari, A. F.; Stella, L.; Turkmen, C.; Zhang, X.; Mercado, P.; Shen, H.; Shchur, O.; Rangapuram, S. S.; Arango, S. P.; Kapoor, S.; et al. 2024. Chronos: Learning the language of time series. *arXiv preprint arXiv:2403.07815*.

Auer, A.; Podest, P.; Klotz, D.; Böck, S.; Klambauer, G.; and Hochreiter, S. 2025. TiRex: Zero-Shot Forecasting Across Long and Short Horizons with Enhanced In-Context Learning. *arXiv preprint arXiv:2505.23719*.

Barnes, R. 2016. *RichDEM: Terrain Analysis Software*.

Bates, E. M.; Lombard, P. B.; et al. 1978. Evaluation of temperature inversions and wind machine on frost protection in southern Oregon. Technical report, Oregon State University.

Beck, M.; Pöppel, K.; Spanring, M.; Auer, A.; Prudnikova, O.; Kopp, M.; Klambauer, G.; Brandstetter, J.; and Hochreiter, S. 2024. xlstm: Extended long short-term memory. *Advances in Neural Information Processing Systems*, 37: 107547–107603.

Bish, M. D.; Guinan, P. E.; and Bradley, K. W. 2019. Inversion climatology in high-production agricultural regions of Missouri and implications for pesticide applications. *Journal of Applied Meteorology and Climatology*, 58(9): 1973–1992.

Burger, M.; Gubler, M.; and Brönnimann, S. 2022. Modeling the intra-urban nocturnal summertime air temperature fields at a daily basis in a city with complex topography. *PLOS Climate*, 1(12): e0000089.

Canché-Cab, L.; San-Pedro, L.; Ali, B.; Rivero, M.; and Escalante, M. 2024. The atmospheric boundary layer: a review of current challenges and a new generation of machine learning techniques. *Artificial Intelligence Review*, 57(12): 331.

Chu, Y.; Lin, G.; Deng, M.; Xue, L.; Li, W.; Shin, H. H.; Zhang, J. A.; Guo, H.; and Wang, Z. 2025. Machine Learning Model for Inverting Convective Boundary Layer Height with Implicit Physical Constraints and Its Multi-Site Applicability. *EGUsphere*, 2025: 1–38.

Das, A.; Kong, W.; Sen, R.; and Zhou, Y. 2024. A decoder-only foundation model for time-series forecasting. In *Forty-first International Conference on Machine Learning*.

Dennstaedt, S. 2023. What Do Pilots Need to Know About Temperature Inversions? https://www.flyingmag.com/what-do-pilots-need-to-know-about-temperature-inversions/. Accessed: August 18, 2025.

Ekambaram, V.; Jati, A.; Dayama, P.; Mukherjee, S.; Nguyen, N.; Gifford, W. M.; Reddy, C.; and Kalagnanam, J. 2024. Tiny time mixers (ttms): Fast pre-trained models for enhanced zero/few-shot forecasting of multivariate time series. *Advances in Neural Information Processing Systems*, 37: 74147–74181.

Gommes, R.; Das, H.; Mariani, L.; Challinor, A.; Tychon, B.; Balaghi, R.; and Dawod, M. 2010. *Agrometeorological forecasting*. Geneva (Switzerland): World Meteorological Organization (WMO).

Haby, J. 2024. Planetary Boundary Layer. https://www.weather.gov/source/zhu/ZHU_Training_Page/clouds/planetary_boundary_layer/PBL.html.

Haynes, K.; Stock, J.; Dostalek, J.; Anderson, C.; and Ebert-Uphoff, I. 2024. Exploring the Use of Machine Learning to Improve Vertical Profiles of Temperature and Moisture. *Artificial Intelligence for the Earth Systems*, 3(1): e220090.

Helbig, M.; Gerken, T.; Beamesderfer, E. R.; Baldocchi, D. D.; Banerjee, T.; Biraud, S. C.; Brown, W. O.; Brunsell, N. A.; Burakowski, E. A.; Burns, S. P.; Butterworth, B. J.; Chan, W. S.; Davis, K. J.; Desai, A. R.; Fuentes, J. D.; Hollinger, D. Y.; Kljun, N.; Mauder, M.; Novick, K. A.; Perkins, J. M.; Rahn, D. A.; Rey-Sanchez, C.; Santanello, J. A.; Scott, R. L.; Seyednasrollah, B.; Stoy, P. C.; Sullivan, R. C.; De Arellano, J. V.-G.; Wharton, S.; Yi, C.; and Richardson, A. D. 2021. Integrating continuous atmospheric boundary layer and tower-based flux measurements to advance understanding of land-atmosphere interactions. *Agricultural and Forest Meteorology*, 307: 108509.

Hiscox, A.; Bhimireddy, S.; Wang, J.; Kristovich, D. A. R.; Sun, J.; Patton, E. G.; Oncley, S. P.; and Brown, W. O. J. 2023. Exploring Influences of Shallow Topography in Stable Boundary Layers: The SAVANT Field Campaign. *Bulletin of the American Meteorological Society*, 104(2): E520–E541.

Hochreiter, S.; and Schmidhuber, J. 1997. Long short-term memory. *Neural computation*, 9(8): 1735–1780.

Hudson, S. R.; and Brandt, R. E. 2005. A Look at the Surface-Based Temperature Inversion on the Antarctic Plateau. *Journal of Climate*, 18(11): 1673–1696.

Jin, M.; Koh, H. Y.; Wen, Q.; Zambon, D.; Alippi, C.; Webb, G. I.; King, I.; and Pan, S. 2024. A Survey on Graph Neural Networks for Time Series: Forecasting, Classification, Imputation, and Anomaly Detection. *IEEE Transactions on Pattern Analysis and Machine Intelligence*, 46(12): 10466–10485.

Joly, D.; and Richard, Y. 2022a. Temperature inversions in France – Part A: time variations. *Climatologie*, 19: 4.

Joly, D.; and Richard, Y. 2022b. Temperature inversions in France – Part B: Spatial variations. *Climatologie*, 19: 5.

Kingma, D. P.; and Ba, J. 2017. Adam: A Method for Stochastic Optimization. arXiv:1412.6980.

Kumar, N.; Soni, K.; and Agarwal, R. 2021. Prediction of temporal atmospheric boundary layer height using long short-term memory network. *Tellus A: Dynamic Meteorology and Oceanography*, 73(1): 1926132.

Lagmiri, S.; and Dahech, S. 2024. Temperature Inversion and Particulate Matter Concentration in the Low Troposphere of Cergy-Pontoise (Parisian Region). *Atmosphere*, 15(3): 349.

LeCun, Y.; Bengio, Y.; and Hinton, G. 2015. Deep learning. *nature*, 521(7553): 436–444.

Ma, Z.; Li, Z.; Li, J.; Schmit, T. J.; Cucurull, L.; Atlas, R.; and Sun, B. 2021. Enhance Low Level Temperature and Moisture Profiles Through Combining NUCAPS, ABI Observations, and RTMA Analysis. *Earth and Space Science*, 8(6): e2020EA001402.

Milstein, A. B.; Santanello, J. A.; and Blackwell, W. J. 2023. Detail Enhancement of AIRS/AMSU Temperature and Moisture Profiles Using a 3D Deep Neural Network. *Artificial Intelligence for the Earth Systems*, 2(2): 220037.

Noad, N. C.; Bonnaventure, P. P.; Gilson, G. F.; Jiskoot, H.; and Garibaldi, M. C. 2023. Surface-based temperature inversion characteristics and impact on surface air temperatures in northwestern Canada from radiosonde data between 1990 and 2016. *Arctic Science*, 9(3): 545–563.

Novick, K. A.; Oishi, A. C.; and Miniat, C. F. 2016. Cold air drainage flows subsidize montane valley ecosystem productivity. *Global Change Biology*, 22(12): 4014–4027.

Ohlemeier, D. 2025. Washington State System helps with Orchard Frost Protection - Fruit Growers News. https://fruitgrowersnews.com/article/washington-state-system-helps-with-orchard-frost-protection/.

Pielke Sr, R. A. 2013. *Climate vulnerability: understanding and addressing threats to essential resources*. Elsevier.

Prengaman, K. 2025. Inversion conditions help inform Frost forecasts. https://goodfruit.com/inversion-conditions-help-inform-frost-forecasts/.

Ramsey, E.; and Monahan, A. H. 2022. Empirical Low-Dimensional Dynamics of Atmospheric Stable Boundary Layer Temperature Inversions. *Journal of the Atmospheric Sciences*, 79(7): 1965–1984.

Rendón, A. M.; Salazar, J. F.; Palacio, C. A.; Wirth, V.; and Brötz, B. 2014. Effects of Urbanization on the Temperature Inversion Breakup in a Mountain Valley with Implications for Air Quality. *Journal of Applied Meteorology and Climatology*, 53(4): 840–858.

Riordan, A. J.; Davis, J. M.; and Kiess, R. B. 1986. The morning inversion near the ground and its daytime transition at two rural sites in the Carolinas. *Journal of Applied Meteorology and Climatology*, 25(2): 239–256.

Rupp, D. E.; Shafer, S. L.; Daly, C.; Jones, J. A.; and Frey, S. J. 2020. Temperature gradients and inversions in a forested Cascade Range basin: Synoptic-to local-scale controls. *Journal of Geophysical Research: Atmospheres*, 125(23): e2020JD032686.

Silva, P. R. P.; Carneiro, R. G.; Moraes, A. O.; Dias-Junior, C. Q.; and Fisch, G. 2025. Estimating Planetary Boundary Layer Height over Central Amazonia Using Random Forest. *Atmosphere*, 16(8): 941.

Srivastava, N.; Hinton, G.; Krizhevsky, A.; Sutskever, I.; and Salakhutdinov, R. 2014. Dropout: a simple way to prevent neural networks from overfitting. *The journal of machine learning research*, 15(1): 1929–1958.

Su, T.; and Zhang, Y. 2024. Deep-learning-derived planetary boundary layer height from conventional meteorological measurements. *Atmospheric Chemistry and Physics*, 24(11): 6477–6493.

Survey, U. G. 2024. Annual NLCD (National Land Cover Database) Collection 1 Science Products. Accessed: 2025-08-16.

Survey, U. S. G. 2021. 3D Elevation Program 1/3-arc-second Digital Elevation Model. Distributed by OpenTopography. Accessed 2025-07-10.

Sutskever, I.; Vinyals, O.; and Le, Q. V. 2014. Sequence to Sequence Learning with Neural Networks. ArXiv:1409.3215 [cs].

Vaswani, A.; Shazeer, N.; Parmar, N.; Uszkoreit, J.; Jones, L.; Gomez, A. N.; Kaiser, L.; and Polosukhin, I. 2017. Attention Is All You Need. arXiv:1706.03762.

Wen, Q.; Zhou, T.; Zhang, C.; Chen, W.; Ma, Z.; Yan, J.; and Sun, L. 2022. Transformers in time series: A survey. *arXiv preprint arXiv:2202.07125*.

Williams, R. J.; and Zipser, D. 1989. A learning algorithm for continually running fully recurrent neural networks. *Neural computation*, 1(2): 270–280.

Wu, C.; Zhao, Y.; Wu, P.; and Deng, X. 2024. Circumferential Background Field Temperature Inversion Prediction and Correction Based on Ground-Based Microwave Remote Sensing Data. *Journal of Marine Science and Engineering*, 12(12): 2344.

Xu, T.; Liu, B.; Zhang, M.; Song, Y.; Kang, L.; Wang, T.; Liu, M.; Cai, X.; Zhang, H.; and Zhu, T. 2021. Temperature inversions in China derived from sounding data from 1976 to 2015. *Tellus B: Chemical and Physical Meteorology*, 73(1): 1898906.

Xu, T.; Song, Y.; Liu, M.; Cai, X.; Zhang, H.; Guo, J.; and Zhu, T. 2019. Temperature inversions in severe polluted days derived from radiosonde data in North China from 2011 to 2016. *Science of the Total Environment*, 647: 1011–1020.

Yang, W.; Liu, L.; Deng, W.; Huang, W.; Ye, J.; and Hu, S. 2023. Deep Retrieval Architecture of Temperature and Humidity Profiles from Ground-Based Infrared Hyperspectral Spectrometer. *Remote Sensing*, 15(9): 2320.

Zeng, H.; Tian, P.; Zhang, M.; Cao, X.; Liang, J.; and Zhang, L. 2022. Rapid change in surface-based temperature inversions across the world during the last three decades. *Journal of Applied Meteorology and Climatology*, 61(2): 175–184.

Zhang, D.; Comstock, J.; Sivaraman, C.; Mo, K.; Krishnamurthy, R.; Tian, J.; Su, T.; Li, Z.; and Roldán-Henao, N. 2025a. Best Estimate of the Planetary Boundary Layer Height from Multiple Remote Sensing Measurements. https://egusphere.copernicus.org/preprints/2025/egusphere-2024-3959/.

Zhang, D.-P.; Gu, W.-B.; Esamdin, A.; Bai, C.-H.; Niu, H.-B.; Liu, L.-Y.; and Zhang, J.-C. 2025b. Characteristics of Surface Temperature Inversion at the Muztagh-Ata Site on the Pamir Plateau. *Atmosphere*, 16(8): 897.

Zhang, Y.; Zhang, B.; and Yang, N. 2022. Characteristics of Temperature and Humidity Inversions Based on High-Resolution Radiosonde Observations at Three Arctic Stations. *Journal of Applied Meteorology and Climatology*, 61(4): 415–428.